Article

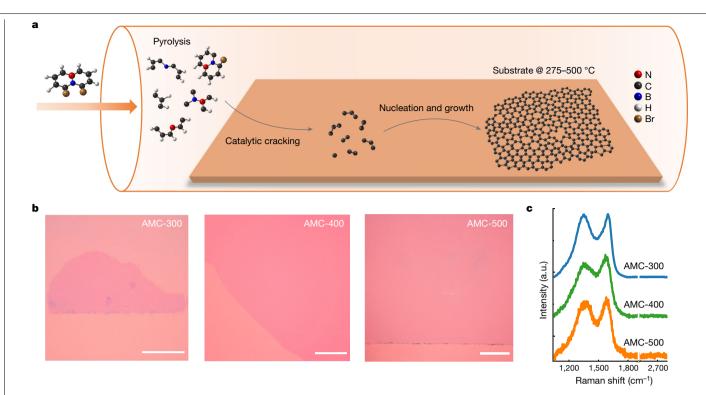# Disorder-tuned conductivity in amorphous monolayer carbon

Huifeng Tian[1,18], Yinhang Ma[2,18], Zhenjiang Li[1,18], Mouyang Cheng[3,18], Shoucong Ning[4,18], Erxun Han[3], Mingquan Xu[2], Peng-Fei Zhang[5], Kexiang Zhao[5], Ruijie Li[1], Yuting Zou[6], PeiChi Liao[1], Shulei Yu[1], Xiaomei Li[6], Jianlin Wang[6], Shizhuo Liu[1], Yifei Li[1], Xinyu Huang[1,7], Zhixin Yao[1,8], Dongdong Ding[3], Junjie Guo[8], Yuan Huang[7], Jianming Lu[3], Yuyan Han[9], Zhaosheng Wang[9], Zhi Gang Cheng[6,10], Junjiang Liu[10], Zhi Xu[10], Kaihui Liu[3,10,11], Peng Gao[10,11,12], Ying Jiang[11,12], Li Lin[1], Xiaoxu Zhao[1], Lifen Wang[6,10], Xuedong Bai[6,10], Wangyang Fu[13], Jie-Yu Wang[5], Maozhi Li[14], Ting Lei[1], Yanfeng Zhang[1], Yanglong Hou[1], Jian Pei[5], Stephen J. Pennycook[2,4], Enge Wang[10,11,12,15], Ji Chen[3,11,16✉], Wu Zhou[2,17✉] & Lei Liu[1,11✉]

Correlating atomic configurations—specifically, degree of disorder (DOD)—of an amorphous solid with properties is a long-standing riddle in materials science and condensed matter physics, owing to difficulties in determining precise atomic positions in 3D structures[1–5]. To this end, 2D systems provide insight to the puzzle by allowing straightforward imaging of all atoms[6,7]. Direct imaging of amorphous monolayer carbon (AMC) grown by laser-assisted depositions has resolved atomic configurations, supporting the modern crystallite view of vitreous solids over random network theory[8]. Nevertheless, a causal link between atomic-scale structures and macroscopic properties remains elusive. Here we report facile tuning of DOD and electrical conductivity in AMC films by varying growth temperatures. Specifically, the pyrolysis threshold temperature is the key to growing variable-range-hopping conductive AMC with medium-range order (MRO), whereas increasing the temperature by 25 °C results in AMC losing MRO and becoming electrically insulating, with an increase in sheet resistance of 10^9 times. Beyond visualizing highly distorted nanocrystallites embedded in a continuous random network, atomic-resolution electron microscopy shows the absence/presence of MRO and temperature-dependent densities of nanocrystallites, two order parameters proposed to fully describe DOD. Numerical calculations establish the conductivity diagram as a function of these two parameters, directly linking microstructures to electrical properties. Our work represents an important step towards understanding the structure–property relationship of amorphous materials at the fundamental level and paves the way to electronic devices using 2D amorphous materials.

The 'microstructure determines properties' model has been very successful in explaining and predicting behaviours of crystalline materials and purposely manipulating the properties of materials[9,10]. However, apart from the challenge in determining the precise atomic positions, 3D glassy materials exhibit considerably diverse structural features in short-to-medium-range ordering[1–3,11]. Moreover, disorder types and DOD exhibit notoriously complex behaviours with temperature, composition or even processing history, severely hampering a causal link between critical structural features and macroscopic properties[4,5]. In 2D systems, because of the reduced structural complexity in the z direction, structural puzzles of amorphousness could potentially be addressed by direct imaging of all atoms[8,12,13]. Structures of vitreous monolayer silica and carbon have been successfully resolved atom by atom in 2D space[8,14]. However, to decipher how micro-disorder influences macroscopic properties in 2D amorphous materials, the practical tuning of both atomic arrangements and properties is a prerequisite,

[1]School of Materials Science and Engineering, Peking University, Beijing, China. [2]School of Physical Sciences, CAS Key Laboratory of Vacuum Physics, University of Chinese Academy of Sciences, Beijing, China. [3]School of Physics, Peking University, Beijing, China. [4]Department of Materials Science and Engineering, National University of Singapore, Singapore, Singapore. [5]Beijing National Laboratory for Molecular Sciences, College of Chemistry and Molecular Engineering, Peking University, Beijing, China. [6]Beijing National Laboratory for Condensed Matter Physics, Institute of Physics, Chinese Academy of Sciences, Beijing, China. [7]Advanced Research Institute of Multidisciplinary Science, Beijing Institute of Technology, Beijing, China. [8]Key Laboratory of Interface Science and Engineering in Advanced Materials, Ministry of Education, Taiyuan University of Technology, Taiyuan, China. [9]Anhui Province Key Laboratory of Condensed Matter Physics at Extreme Conditions, High Magnetic Field Laboratory, Chinese Academy of Sciences, Hefei, China. [10]Songshan Lake Materials Laboratory, Dongguan, China. [11]Interdisciplinary Institute of Light-Element Quantum Materials and Research Center for Light-Element Advanced Materials, Peking University, Beijing, China. [12]International Center for Quantum Materials, Collaborative Innovation Center of Quantum Matter, Peking University, Beijing, China. [13]School of Materials Science and Engineering, Tsinghua University, Beijing, China. [14]Department of Physics, Beijing Key Laboratory of Opto-electronic Functional Materials and Micro-Nano Devices, Renmin University of China, Beijing, China. [15]School of Physics, Liaoning University, Shenyang, China. [16]Frontiers Science Center for Nano-Optoelectronics, Peking University, Beijing, China. [17]CAS Center for Excellence in Topological Quantum Computation, University of Chinese Academy of Sciences, Beijing, China. [18]These authors contributed equally: Huifeng Tian, Yinhang Ma, Zhenjiang Li, Mouyang Cheng, Shoucong Ning. ✉e-mail: ji.chen@pku.edu.cn; wuzhou@ucas.ac.cn; l_liu@pku.edu.cn

Fig. 1 | Low-temperature CVD growth of AMC on Cu foils. a, Schematic of the growth using BN-doped 1,8-dibromonaphthalene as the precursor. By the pyrolysis, the precursor was decomposed to small species such as A3 (containing three atoms of B, C or N, and several H atoms), which was confirmed by the pyrolysis–gas chromatography–mass spectrometry measurements. The growth

consists of the surface-mediated molecule cracking and a subsequent nucleation-growth process. **b**, Representative optical microscopy images of AMC-300, AMC-400 and AMC-500 films after transfer onto SiO$_2$/Si substrates. Scale bars, 200 μm. **c**, Raman spectra of AMC samples, showing broad D and G peaks and the complete absence of the G′ band.

but remains elusive. Herein we report the chemical vapour deposition (CVD) synthesis of AMC with distinct DOD by simply varying growth temperatures, enabling the quantitative correlation of atomic arrangements with electrical properties.

Figure 1a sketches the CVD growth of AMC from heteroaromatic molecules. Compared with the laser-assisted dissociation of precursors[8], during thermal CVD, the main parameter governing the precursor decomposition is the substrate temperature, which can be accurately controlled, enabling much more precise control of the precursor cracking, subsequent nucleation and growth. For the growth of crystalline monolayer carbon (graphene), the thermal CVD has been widely investigated through the precursor pyrolysis (>650 °C)[15–18] or self-assembling cyclic aromatic molecules without rings breaking (typically <500 °C)[19–24] (Supplementary Table 1). To accomplish the bottom-up growth of AMC, a polycyclic heteroarene, boron nitride (BN)-doped 1,8-dibromonaphthalene[25], was selected as the precursor (Extended Data Fig. 1).

Growth over a wide temperature range (200–800 °C) showed routine temperature-dependent growth behaviours, with the onset growth temperature at 275 °C (Extended Data Fig. 2). Although irregular-shaped films of more than hundreds of microns (AMC-300) were obtained along Cu foil edges at 300 °C, full-coverage, continuous AMC-400 and AMC-500 films were consistently synthesized at higher temperatures (Fig. 1b). Raman measurements of AMC samples show broad D and G peaks without G′ signal (Fig. 1c), suggesting a high level of structural disorder[26]. In contrast to the finite coverages of AMC-300, AMC-325 showed full coverage on Cu foils with a much higher growth velocity, manifesting the growth mutation within 25 °C. AMC samples synthesized above 500 °C had some bilayer regions, indicating the absence of the self-limited growth[15] (Extended Data Fig. 2). As control experiments, AMC′ samples were grown with 1,8-dibromonaphthalene as precursors (Extended Data Fig. 3), which showed a higher threshold

temperature (350 °C) and only continuous films with full coverages. These findings highlight the decisive role of the B/N incorporation in precursors on relatively lower temperatures of precursor decomposition and amorphous monolayer growth (Supplementary Note 1), consistent with theoretical calculations of the cracking routes of precursors (Extended Data Fig. 4).

Figure 2a shows selected-area electron diffraction (SAED) patterns acquired over regions of a few micrometres for different AMC samples. The diffuse halos and the absence of diffraction spots in SAED patterns indicate the amorphous feature in all samples, whereas halos of AMC-400 are more diffuse, suggesting a higher DOD. By using four-dimensional scanning transmission electron microscopy (4D-STEM) nanobeam electron diffraction (NBED), we further reduce the characterization scale to a few nanometres. Figure 2b–d shows the averaged NBED patterns for two adjacent subregions of 6 × 6 nm^2 in three AMC samples. In Fig. 2b, the left panel shows a diffuse halo and the right panel contains several broad first-order and second-order diffraction spots as well as the diffuse halos, indicating an inhomogeneous spatial distribution of nanocrystallites and glassy structures in AMC-300 at the scale of 6 nm. Unlike AMC-300, the region-averaged NBED pattern of AMC-400 at the same scale predominantly shows diffuse halos (Fig. 2c) and for AMC-500, only blurry spots are observed with halos (Fig. 2d), indicating the temperature-dependent differences in DOD at the scale of sub-10 nm. Moreover, the averaged NBED patterns of various sizes of subregions (Extended Data Figs. 5–7) show that, when the size of the region is increased from 6 × 6 nm^2 to 36 × 36 nm^2, the NBED patterns of all samples turn into diffuse halos similar to the SAED patterns, indicating the absence of long-range order.

Representative atomic-resolution annular dark-field scanning transmission electron microscopy (ADF-STEM) images are shown in Fig. 2e–g. All AMC samples show continuous networks composed of threefold-coordinated *sp*^{2}-like carbon. To quantitatively describe the
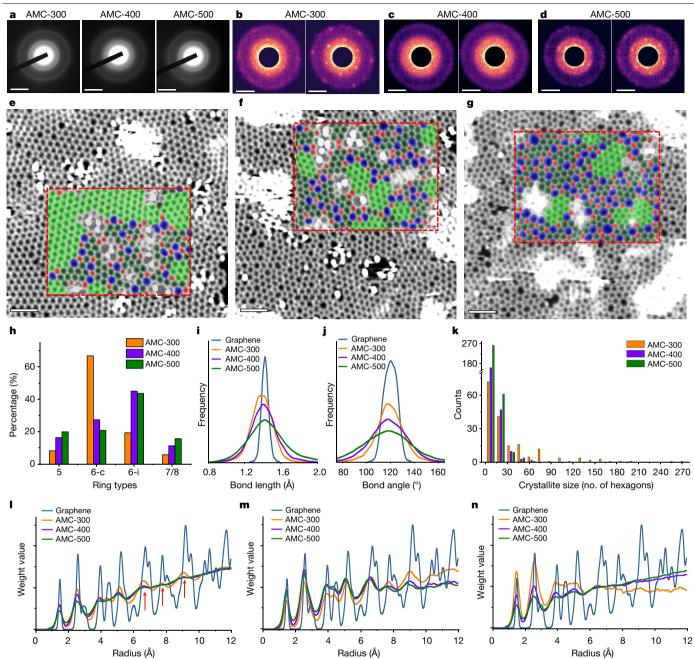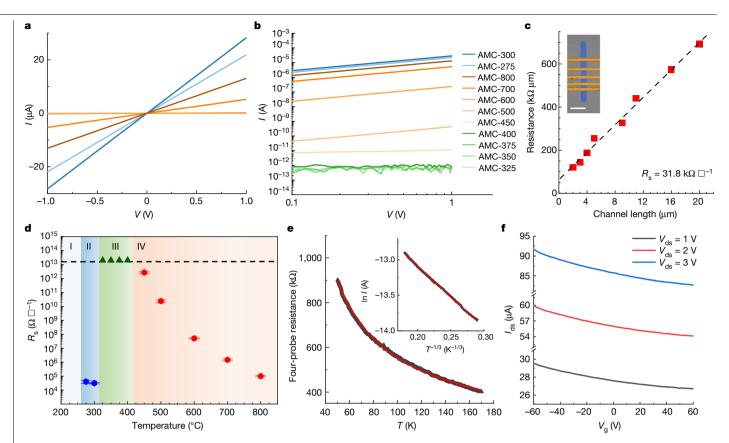
Fig. 2 | Atomic-scale structural characterizations of AMC. a, SAED patterns of AMC-300, AMC-400 and AMC-500 samples acquired over micrometre-sized regions. All diffraction patterns show diffused halos, whereas the halos are more diffuse for AMC-400. **b–d**, Representative NBED patterns of two adjacent regions (6×6 nm^2) for AMC-300 (**b**), AMC-400 (**c**) and AMC-500 (**d**), respectively. **e–g**, Representative denoised ADF-STEM images of AMC-300 (**e**), AMC-400 (**f**) and AMC-500 (**g**), with colour-coded overlays in areas highlighted by red rectangles. Hexagonal carbon rings in crystallite and isolated regions are highlighted in bright green and dark green, respectively, in which only the area equal to or larger than a hexagon surrounded by six hexagons is considered as one crystallite. Pentagonal carbon rings are filled with red and heptagonal and octagonal rings are filled with blue. **h**, Statistics of the percentages of pentagons (5), crystalline hexagons (6-c), isolated hexagons (6-i) and heptagons/octagons (7/8). **i,j**, Statistics of bond-length distributions (**i**) and bond-angle distributions (**j**). **k**, Statistics of the size distribution of crystallites, in terms of the number of hexagons. **l–n**, Pair distribution functions $g(r)$ of the carbon atoms in the entire regions (**l**), in crystalline regions with radius >1.2 nm (**m**) and in non-crystalline (CRN) regions with radius >1.2 nm (**n**), obtained from experimental ADF-STEM images of conventional CVD-grown graphene, AMC-300, AMC-400 and AMC-500 samples, respectively. In **l**, among the AMC samples, MRO in the range 6–10 Å only exists for AMC-300 (highlighted by arrows). No marked differences in the $g(r)$ are observed in **m** and **n**, indicating that MRO is present in the crystalline areas but absent in CRN regions for all samples. The MRO difference between AMC-300 and AMC-400/AMC-500 is thus determined by the higher ratio of crystalline to CRN areas in AMC-300. In **h–n**, 32 randomly selected ADF-STEM images were used. Scale bars, 5 nm^{-1} (**a–d**), 1 nm (**e–g**).

amorphous structures, we first mapped different types of carbon ring by colours (Fig. 2e–g), in which the pentagons, heptagons/octagons and hexagons are highlighted in red, blue and green, respectively. For hexagons, bright and dark green are used to differentiate hexagonal carbon rings in the crystallite and isolated areas (denoted as 6-c and 6-i,

respectively. Although all samples show graphene-like nanocrystallites surrounded by continuous random network (CRN) regions[8,27], one can see that AMC-300 contains larger crystallites and fewer CRN regions as compared with AMC-400 and AMC-500 (Extended Data Fig. 8). Figure 2h shows the statistics of different types of carbon ring calculated from

Fig. 3 | Electrical characterizations of AMC. a,b, Two-terminal I–V measurements in a linear (**a**) and logarithmic (**b**) plot, showing the very different conducting behaviour of AMC, including the insulating ones (green), highly conductive ones (blue) and intermediate ones (orange). **c**, Multi-terminal device measurements using the TLM for one AMC-300 device to obtain R_s with consideration of the contact resistance. Inset, a false-colour optical image of the device. Scale bar, 10 μm. **d**, Conductivity diagram for AMC as a function of temperature, showing the four different zones. The dashed line indicates the detection limit of the

instrument. The number of devices at each temperature is $n = 10$, and the error bars show standard deviation. **e**, Four-probe resistance (black triangles) versus temperature, showing the semiconducting behaviour for AMC-300 devices. The red line is the fitting to Mott's 2D variable-range-hopping model ($\rho(T) \propto \exp[(T_0/T)^{\frac{1}{3}}]$)[31,32]. Inset, natural logarithm of the current as a function of $T^{-1/3}$. **f**, Typical transfer curves of field-effect transistors under different bias voltages, showing slight p-type behaviours.
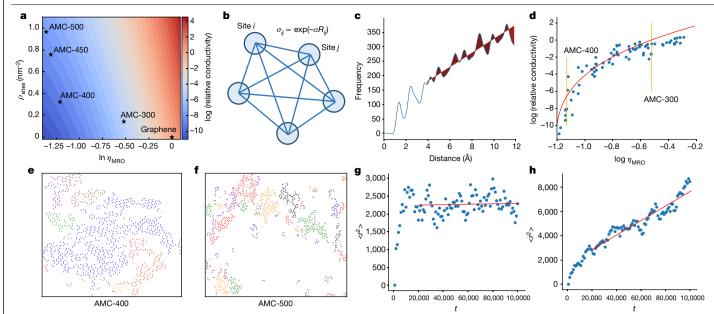
32 randomly selected ADF-STEM images. The hexagons constitute about 86% of the carbon rings in AMC-300, with most (about 67%) in nanocrystallites and about 19% as isolated hexagons. By contrast, AMC-400 contains more isolated hexagons (about 45%) and more 5/7/8 rings (about 28%), demonstrating a higher DOD in AMC-400, whereas AMC-500 exhibits comparable proportions of isolated hexagons (about 44%) with AMC-400 but slightly more non-six-membered rings (about 36%). For the statistics of bond length and bond angle based on 2D projections seen in the ADF-STEM images (Fig. 2i,j), all AMC samples show broad distributions of bond lengths and angles, which are much more diffuse than those of graphene, indicating the high degree of structural distortion in AMC samples. Although AMC-500 possesses more distorted structures, both AMC-500 and AMC-400 clearly have broader distributions in the bond length and bond angle than those of AMC-300, suggesting higher DOD in AMC-400 and AMC-500 that is consistent with the electron diffraction results.

The distribution of crystallite sizes, in terms of the number of hexagons in each nanocrystallite, is shown in Fig. 2k. Compared with AMC-300, the distributions of crystallite size in AMC-400 and AMC-500 shift to the lower range and no crystallites with sizes larger than 70 hexagons were detected, whereas nanocrystallites as large as 270 hexagons (equivalent to a diameter of approximately 3.5 nm) were found in AMC-300, though only a small portion. AMC-500 manifests smaller and denser nanocrystallites than AMC-400. Moreover, the structure of AMC-450 was analysed in the same manner (Fig. S4) and the size and density of nanocrystallites are between those of AMC-400 and

AMC-500, suggesting the temperature tuning of the distribution of crystallite size.

Pair distribution functions $g(r)$, calculated from distances between carbon atom pairs in experimental ADF-STEM images, are further evaluated[1,28]. As shown in Fig. 2l, for overall $g(r)$ (for entire monolayer regions), in contrast to the distinct and sharp peaks in $g(r)$ for graphene, AMC samples show much broader peaks in $g(r)$. Notably, whereas all AMC samples hold similar short-range order (SRO), their $g(r)$ show very different behaviours in the 6–10-Å range. Specifically, weak MRO is observed only in AMC-300 with three broad peaks marked by red arrows, whereas MRO is absent in AMC-400 and AMC-500 (and AMC-450, Fig. S4g). To understand the origins of the presence/absence of MRO in AMC, we further analysed $g(r)$ separately for nanocrystalline and CRN regions greater than 1.2 in size. For crystalline regions (Fig. 2m), all samples show clear SRO and weak MRO, with broad peaks retained in the 6–10-Å range, whereas CRN regions (Fig. 2n) only show SRO without any peaks in the MRO range. The analysis thus indicates that the ratio of the crystalline and non-crystalline regions, as well as their spatial distributions, determines the overall $g(r)$ (Fig. 2l), which is consistent with the analysis of SAED/NBED patterns (Fig. 2a–d) and ring types (Fig. 2h).

To explore whether the DOD discrepancies can be translated into chemical/physical properties, thermostability in air and electrical measurements on AMC have been performed. By heating AMC samples with laser irradiations and simultaneously tracking the evolution of Raman spectra (Extended Data Fig. 9), we found that AMC-400 had

Fig. 4 | Theoretical analysis of the relationship between DOD and conductivity in AMC. a, Conductivity diagram as a function of the level of MRO η_{MRO} and the average density of hopping sites ρ_{sites} based on the theoretical calculations. For graphene, AMC-300, AMC-400, AMC-450 and AMC-500, the conductivity and two order parameters can be derived from experiments and match well with theory. **b**, Schematics of the hopping conduction model, in which the circles indicate conducting sites. **c**, The definition of A_{MRO}. The blue line is one $g(r)$ from STEM images and the red line shows a linear fit of the blue line from 4 to 12 Å. The shaded region indicates the difference between the blue line and the red line, and the area of the shaded region is defined as A_{MRO}. The level of MRO is defined as the ratio between A_{MRO} of AMC and graphene, namely $\eta_{MRO} = \frac{A_{MRO}\,(AMC)}{A_{MRO}\,(graphene)}$. **d**, Relative conductivity to graphene as a function of MRO, plotted with double logarithmic axes. Vertical lines represent values of η_{MRO} corresponding to AMC-300 and AMC-400, which were calculated using experimentally observed structures, predicting seven orders of magnitude difference in conductivity. **e,f**, Patterns of conducting sites for AMC-400 and AMC-500, respectively. Only crystalline regions are plotted, and differently coloured clusters indicate discrete hopping sites. **g,h**, Monte Carlo simulations of electron hopping for AMC-400 and AMC-500, respectively. The blue dots are mean square displacements $<r^2>$ as a function of simulation time and the red lines are corresponding linear fits, in which the electronic conductivity is indicated by the slope according to Einstein's relation. The saturation of $<r^2>$ for AMC-400 indicates the electron localization within conducting sites and, consequently, insulating.

the poorest thermal stability, whereas AMC-300 exhibited the highest stability, in consonance with DOD differences[29]. As shown in Fig. 3a,b for I–V curves of two-terminal AMC devices (Supplementary Table 3), AMC samples can be classified into three groups by electrical conductivities, showing a conductor-to-insulator transition and continuous tuning of conductivities. Using the transmission line method (TLM), we obtained the sheet resistance R_s of conductive AMC samples after deducting contact resistances (Fig. 3c and Extended Data Fig. 10) and plotted R_s as a function of growth temperature (Fig. 3d), which was naturally divided into four zones. In zone I (<275 °C), no AMC sample can be grown. Highly conductive AMC with R_s as low as 32 kΩ □⁻¹, presence of MRO and finite coverage were prepared in zone II (275–300 °C). Notably, by only increasing 25 °C, AMC jumped into zone III (300 °C < T ≤ 400 °C), with an increase of R_s by nine orders of magnitude (beyond the detection limit of our instruments; Extended Data Fig. 11), the absence of MRO and full coverage. AMC samples in zone IV (>400 °C) manifest the tunable R_s with a negative temperature correlation and smaller, denser nanocrystallites (Figs. S5–S7). With the same molecule precursor and growth procedure, we show one-billion-fold enhancement in electrical conductivities of amorphous monolayers by simply varying the growth temperature (325 °C to 300 °C), and further tuning the growth temperature can continuously fill the gap between these two limits. For bulk amorphous materials, changing the synthesis temperature by 25 °C normally does not affect their properties, not to mention the modulation of electric properties[30], demonstrating unprecedented advantages of tuning DOD in 2D amorphous materials. Furthermore, four-probe resistance measurements (Fig. 3e) show that AMC-300 behaves as a classical semiconductor, with the resistance decreasing on increasing temperature. The natural logarithm of the current shows a linear dependence on $T^{-1/3}$ (inset of Fig. 3e), indicating the 2D

variable-range-hopping conduction for AMC-300 (refs. [31–33]) (and zone IV AMC samples; Extended Data Fig. 10g).

To understand the AMC conductivity and its relation to DOD, systematic theoretical analyses were carried out. We performed density functional theory calculations on the nanocrystalline region and CRN region (Supplementary Note 2). Calculations show that, although conduction bands can form in both structures, the ordered nanocrystalline region is probably more conducting and the disordered CRN region dominated by non-six-membered rings is more insulating. Such analysis is consistent with the previous theoretical studies in which ring disorders in AMC substantially change the density of states and reduce electronic conductivity[34,35]. These calculations suggest that we can discuss the conductivity of the whole structure by dividing it into conducting and insulating regions, in which the hopping conductivity model can then be used, as also suggested by experimental measurements[33,36].

We further identified that, when considering electron transport in AMC, the DOD needs to be described by two order parameters, namely the level of MRO and the average density of conducting sites ρ_{sites} (Supplementary Note 3). As shown in Fig. 4a, these two order parameters collectively determine the conductivity of AMC in two dimensions. A random structure generation was designed to reproduce a wide range of structures (Supplementary Note 4) and the hopping conductivity model is sketched in Fig. 4b. The level of MRO is defined by the ratio between the medium-range area in $g(r)$ of AMC and graphene (Fig. 4c). The total conductivity is plotted logarithmically as a function of η_{MRO} (Fig. 4d, Supplementary Note 4 and Supplementary Fig. S9). The conductivity is enhanced by seven to eight orders of magnitude from AMC-400 to AMC-300, which agrees with experimental measurements.

Although MRO in AMC-400 and above is mostly suppressed (Fig. 2i), ρ_{sites} is necessary to characterize DOD. In Fig. 4e,f, we extracted

nanocrystalline regions from atomic images of AMC-400 and AMC-500, showing that AMC-500 contains smaller crystalline regions with a higher density than AMC-400. With larger but sparser conducting regions (lower ρ_{sites}), electrons hop from one region to another with less probability, and can even be shown to be electrically insulating (AMC-400). On the contrary, with higher ρ_{sites}, electrons are able to hop across the whole sample, leading to a ρ_{sites}-dependent conductivity (AMC-500 and above). Monte Carlo simulations were performed to corroborate the proposed mechanism (Supplementary Note 5). In Fig. 4g,h, the mean square displacement $<r^2>$ of electron hopping saturates over time for AMC-400, indicating localized hopping for electrons. The monotonic increase of $<r^2>$ with time shows long-range hopping of electrons as the origin of the electrical conductivity of AMC-500 holding the same level of MRO with the insulating AMC-400.

The conductivity diagram of AMC as a function of η_{MRO} and ρ_{sites} was therefore built theoretically (Fig. 4a), and experimental DOD–conductivity relationships of graphene, AMC-300, AMC-400, AMC-450 and AMC-500 perfectly fitted this theory diagram, substantiating the proposed model. Our study highlights the complexity of DOD, that is, the MRO cannot fully describe the relationship between the electrical conductivity and structural DOD. In previous studies, conductivity of amorphous graphene based on theoretically proposed structures has been calculated using more accurate ab initio approaches, showing that defects and topological disorders can induce Anderson localization and insulating behaviour of AMC[37]. Our studies show a new set of structural models of AMC involving a larger-scale structure, in which theoretical insights on transport properties can be learned further by more accurate calculations. We note that our experimental characterizations and theoretical model of AMC are in 2D space based on a reasonable assumption that puckering effects do not alter electronic structures substantially[38].

In conclusion, amorphous carbon monolayers with distinct DOD and electrical conductivity were synthesized by using heteroaromatics precursors in the thermal CVD. Atomic configurations of amorphous monolayers were well correlated with their macroscopic properties at the fundamental level, benefiting from the precise determination of atom positions in 2D space. Our results provide one real case to establish the structure–property relationship in 2D glassy systems and, meanwhile, can lead to the immediate exploration of ultrathin electronics by, for example, in-plane epitaxial growth, leading to widespread applications based on 2D amorphous carbons[39]. Disorder can also play a critical role in electron localization, leading to superconductor–insulator and metal–insulator transitions[40,41], which does not occur in the present experiments. Further structural transformation driving monolayer carbons to the critical metal–insulator transition point could be an intriguing topic[37].

Online content

Any methods, additional references, Nature Portfolio reporting summaries, source data, extended data, supplementary information, acknowledgements, peer review information; details of author contributions and competing interests; and statements of data and code availability are available at https://doi.org/10.1038/s41586-022-05617-w.

1. Zallen, R. *The Physics of Amorphous Solids* (Wiley, 1983).
2. Miracle, D. B. A structural model for metallic glasses. *Nat. Mater.* **3**, 697–702 (2004).
3. Sheng, H. W., Luo, W. K., Alamgir, F. M., Bai, J. M. & Ma, E. Atomic packing and short-to-medium-range order in metallic glasses. *Nature* **439**, 419–425 (2006).
4. Greer, A. L. in *Physical Metallurgy* 5th edn (eds Laughlin, D. E. & Hono, K.) 305–385 (Elsevier, 2014).
5. Ma, E. Tuning order in disorder. *Nat. Mater.* **14**, 547–552 (2015).
6. Joo, W. J. et al. Realization of continuous Zachariasen carbon monolayer. *Sci. Adv.* **3**, e1601821 (2017).
7. Hong, S. et al. Ultralow-dielectric-constant amorphous boron nitride. *Nature* **582**, 511–514 (2020).
8. Toh, C. T. et al. Synthesis and properties of free-standing monolayer amorphous carbon. *Nature* **577**, 199–203 (2020).
9. Tilley, R. J. D. *Crystals and Crystal Structures* (Wiley, 2006).
10. Schorr, S. & Weidenthaler, C. (eds) *Crystallography in Materials Science: From Structure-Property Relationships to Engineering* (De Gruyter, 2021).
11. Yang, Y. et al. Determining the three-dimensional atomic structure of an amorphous solid. *Nature* **592**, 60–64 (2021).
12. Kotakoski, J., Krasheninnikov, A. V., Kaiser, U. & Meyer, J. C. From point defects in graphene to two-dimensional amorphous carbon. *Phys. Rev. Lett.* **106**, 105505 (2011).
13. Eder, F. R., Kotakoski, J., Kaiser, U. & Meyer, J. C. A journey from order to disorder - atom by atom transformation from graphene to a 2D carbon glass. *Sci. Rep.* **4**, 4060 (2014).
14. Huang, P. Y. et al. Imaging atomic rearrangements in two-dimensional silica glass: watching silica's dance. *Science* **342**, 224–227 (2013).
15. Li, X. et al. Large-area synthesis of high-quality and uniform graphene films on copper foils. *Science* **324**, 1312–1314 (2009).
16. Reina, A. et al. Large area, few-layer graphene films on arbitrary substrates by chemical vapor deposition. *Nano Lett.* **9**, 30–35 (2009).
17. Nandamuri, G., Roumimov, S. & Solanki, R. Chemical vapor deposition of graphene films. *Nanotechnology* **21**, 145604 (2010).
18. Sun, Z. et al. Growth of graphene from solid carbon sources. *Nature* **468**, 549–552 (2010).
19. Cai, J. et al. Atomically precise bottom-up fabrication of graphene nanoribbons. *Nature* **466**, 470–473 (2010).
20. Kolmer, M. et al. Rational synthesis of atomically precise graphene nanoribbons directly on metal oxide surfaces. *Science* **369**, 571–575 (2020).
21. Yazyev, O. V. A guide to the design of electronic properties of graphene nanoribbons. *Acc. Chem. Res.* **46**, 2319–2328 (2013).
22. Jang, J. et al. Low-temperature-grown continuous graphene films from benzene by chemical vapor deposition at ambient pressure. *Sci. Rep.* **5**, 17955 (2015).
23. Choi, J. H. et al. Drastic reduction in the growth temperature of graphene on copper via enhanced London dispersion force. *Sci. Rep.* **3**, 1925 (2013).
24. Wu, T. et al. Continuous graphene films synthesized at low temperatures by introducing coronene as nucleation seeds. *Nanoscale* **5**, 5456–5461 (2013).
25. Zhang, P. F. et al. Parent B_2N_2-perylenes with different BN orientations. *Angew. Chem. Int. Ed.* **60**, 23313–23319 (2021).
26. Malard, L. M., Pimenta, M. A., Dresselhaus, G. & Dresselhaus, M. S. Raman spectroscopy in graphene. *Phys. Rep.* **473**, 51–87 (2009).
27. Zachariasen, W. H. The atomic arrangement in glass. *J. Am. Chem. Soc.* **54**, 3841–3851 (1932).
28. Egami, T. & Billinge, S. J. *Underneath the Bragg Peaks: Structural Analysis of Complex Materials* (Elsevier, 2003).
29. Xu, Z. et al. Electrical conductivity, chemistry, and bonding alternations under graphene oxide to graphene transition as revealed by *in situ* TEM. *ACS Nano* **5**, 4401–4406 (2011).
30. Wang, W. H., Dong, C. & Shek, C. H. Bulk metallic glasses. *Mater. Sci. Eng. R Rep.* **44**, 45–89 (2004).
31. Mott, N. F. & Davis, E. A. *Electronic Processes in Non-crystalline Materials* (Oxford Univ. Press, 2012).
32. Kaiser, A. B., Gomez-Navarro, C., Sundaram, R. S., Burghard, M. & Kern, K. Electrical conduction mechanism in chemically derived graphene monolayers. *Nano Lett.* **9**, 1787–1792 (2009).
33. Ambegaokar, V., Halperin, B. I. & Langer, J. S. Hopping conductivity in disordered systems. *Phys. Rev. B* **4**, 2612–2620 (1971).
34. Kapko, V., Drabold, D. A. & Thorpe, M. F. Electronic structure of a realistic model of amorphous graphene. *Phys. Status Solidi B* **247**, 1197–1200 (2010).
35. Thapa, R., Ugwumadu, C., Nepal, K., Trembly, J. & Drabold, D. A. *Ab initio* simulation of amorphous graphite. *Phys. Rev. Lett.* **128**, 236402 (2022).
36. Mott, N. F. Conduction in non-crystalline materials. III. Localized states in a pseudogap and near extremities of conduction and valence bands. *Philos. Mag.* **19**, 835–852 (1969).
37. Tuan, D. V. et al. Insulating behavior of an amorphous graphene membrane. *Phys. Rev. B* **86**, 121408(R) (2012).
38. Li, Y., Inam, F., Kumar, A., Thorpe, M. F. & Drabold, D. A. Pentagonal puckering in a sheet of amorphous graphene. *Phys. Status Solidi B* **248**, 2082–2086 (2011).
39. Liu, L. et al. Heteroepitaxial growth of two-dimensional hexagonal boron nitride templated by graphene edges. *Science* **343**, 163–167 (2014).
40. Imada, I., Fujimori, A. & Tokura, Y. Metal-insulator transitions. *Rev. Mod. Phys.* **70**, 1039–1263 (1998).
41. Siegrist, T. et al. Disorder-induced localization in crystalline phase-change materials. *Nat. Mater.* **10**, 202–208 (2011).

Article

Methods

Synthesis of molecular precursors

The synthesis of BN-doped 1,8-dibromonaphthalene (product **5**; see Extended Data Fig. 1) was completed in four steps starting from diallylaminoboron dichloride, which can be easily obtained by the reaction of inexpensive and commercially available BCl_3 and diallylamine[25]. Subsequent allylation and ring-closing metathesis mediated by the Grubbs catalyst afford product **3**. Then compound **4** can be achieved at elevated temperatures with 2,3-dicyano-5,6-dichlorobenzoquinone in hexane. Finally compound **5** as the final product can be attained by bromination reaction with $AlBr_3$ and N-bromosuccinimide. 1,8-Dibromonaphthalene (product **6**) is a commercial product (Sigma Aldrich, 764094).

CVD growth of AMC

The 25-μm-thick Cu foils (Alfa Aesar, item no. 046986) were initially cleaned by diluted (16%) HNO_3 and deionized water and then annealed at 1,000 °C in Ar/H_2 (20 vol% H_2) flow for 30 min. Pre-annealed Cu foils were loaded into a tube furnace with the precursors, which were far away from the furnace heating zone. During the whole growth process, an oil-free turbopump station was used to circumvent possible carbon contaminations. The Cu foils were first heated to the desired temperature (for example, 300 °C) in 15 sccm of H_2 and then the precursor crucible was heated to 90 °C by heating tape for 5–30 min. The growth ceased by stopping the evaporation, followed by abruptly cooling down.

Transfer of CVD samples

The as-grown samples were spin-coated with polymethyl methacrylate (PMMA) and then baked at 160 °C for 2 min. After etching off the Cu foil in $FeCl_3$ solution (1 M), a floating PMMA/AMC stack was obtained and then washed by hydrochloric acid solution (36%) and deionized water several times to remove any residual etchant. The PMMA/AMC stack was then scooped up with 285-nm-thick SiO_2/Si substrates or transmission electron microscopy (TEM) grids. PMMA was eventually removed with acetone and trichloromethane. One alternative method to transfer AMC onto a TEM grid is the direct transfer without involving polymers. One quantifoil Au grid was put (faced down) on one AMC/Cu substrate, followed by applying a drop of isopropanol (IPA) to be immersed. By the slow evaporation of IPA, the TEM grid could be contacted with AMC sample, acting as a support for AMC in the subsequent etching and drying process. 1 M $Na_2S_2O_8$ solution was used to etch Cu foil away and, after being washed by deionized water several times, the resulting TEM grid was rinsed by IPA and then naturally dried.

Characterizations

Optical measurements. Raman measurements were performed after the AMC samples were transferred onto SiO_2 substrates. One 532-nm continuous-wave laser was focused onto as-prepared samples by a 100× (NA = 0.9) objective lens. The Raman signals were collected by the same objective using a backscattering configuration and analysed by a triple-grating spectrometer (Horiba, iHR320). X-ray photoelectron spectroscopy (XPS) spectra were measured by an AXIS Supra apparatus (Kratos Analytical Ltd.) and XPS data were analysed with the XPSPEAK software.

Pyrolysis–gas chromatography–mass spectrometry measurements. The pyrolysis–gas chromatography–mass spectrometry measurements were performed using the EGA/PY-3030D pyrolyser (Frontier Lab) together with a GCMS-QP2010 Plus gas chromatograph and mass spectrometer (Shimadzu). In one run, the pyrolyser was first heated to the designed temperature (275 °C, 300 °C, 325 °C, 400 °C, 450 °C, 500 °C, 600 °C, 700 °C and 800 °C) and then 10 mg ± 0.05 mg of precursors was sent into the pyrolyser by a sample cup. After 6–60 s of airtight heating, the pyrolysis products were transferred to a DB-5ms capillary column (30 m × 0.25 mm × 0.25 um) with helium as the carrier gas. After the chromatographic separation, the pyrolysis products were finally sent to the mass spectrometer. The data were recorded and analysed by using GCMSsolution v4.44 software and the intensity of the chromatographic peaks (ratio) was calculated by the integral of the peak area.

SAED and STEM measurements. SAED was conducted in a JEOL 2100Plus transmission electron microscope at 80 kV. The STEM experiments were performed on a monochromated and aberration-corrected Nion U-HERMES100 electron microscope under an accelerating voltage of 60 kV. The sample was transferred onto a microelectromechanical-systems-based heating chip and then baked at 160 °C for 20 h in a high-vacuum chamber before being loaded into the microscope. For the in situ heating experiment, the temperature was increased from 20 °C to 650 °C over 10 min and then kept at 650 °C during STEM analysis. In an alternative heating process, AMC samples were first annealed in the JEOL 2100Plus at 650 °C for 2 h and cooled to room temperature, then quickly transferred into the Nion U-HERMES100 microscope for characterizations at room temperature (Supplementary Table 4). The convergence semi-angle was 32 mrad and the beam current was about 23 pA for STEM imaging and electron energy loss spectroscopy measurement. The collection angles for ADF-STEM and high-angle dark-field scanning transmission electron microscopy images were 44–210 mrad and 75–210 mrad, respectively. The dispersion, scanning pixel size and exposure time were 0.3 eV per channel, 0.33 Å and 300 ms, respectively, for electron energy loss spectroscopy spectrum imaging. The convergence angle was set to 2 mrad and the beam current was about 268 pA for the 4D-STEM NBED experiment. The 4D-STEM datasets were acquired using a complementary metal–oxide–semiconductor (CMOS) camera with a scanning step of 1 nm per pixel and exposure time of 0.8 ms. Raw ADF-STEM images were denoised using a double-Gaussian filter[42]. The coordinates of atoms in the ADF-STEM images were determined using a home-built script (Supplementary Note 6). For the pair distribution function, the distance between every pair of atoms was calculated and the distance distribution was plotted.

Device fabrication and transport measurements. Multi-terminal devices of AMC samples were fabricated on SiO_2/Si chips using the standard microfabrication procedures of electron-beam lithography. Oxygen plasma was used to pattern the samples. Electric contacts were deposited by thermal evaporation (ZHD400) of In (10 nm)/Au (40 nm) and the lift-off process. Two-terminal I–V measurements were carried out by a vacuum probe station using Keithley 2614B SourceMeters. For four-terminal measurements, the devices were loaded into cryostats (Quantum Design PPMS-16 system) and transport measurements were performed using three lock-in amplifiers (SR830) at different temperatures. A constant AC voltage bias was applied between the source and drain and the current through the sample measured, whereas the other two lock-ins measured the longitudinal sheet resistance and the Hall resistivity.

Computational details. The pathway of catalytic cracking of precursor molecules was calculated by density functional theory calculations, performed with the Vienna Ab initio Simulation Package (VASP)[43]. Projector augmented wave potentials[44] were used with an energy cutoff of 400 eV. The PBE exchange-correlation functional[45] was used to describe the intralayer and interlayer interactions in conjunction with the D3 van der Waals corrections of Grimme[46]. An in-plane lattice constant 3.623 Å was used for the Cu(100) slab to model the reaction enthalpy of the splitting of precursors. Supercells were built with a thick vacuum slab (>17 Å) to model the surfaces. A 1 × 1 × 1 and a 6 × 6 × 1 K-points mesh were used for total-energy and density-of-state calculations, respectively. The amorphous monolayer graphene structures

used in calculations of density of states and partial charge densities were built on the basis of experimental measurements and were fully optimized. Numerical calculations of the conductivity were performed with a self-developed Python program. For Monte Carlo simulations of electron hopping, coordinates of atoms were extracted directly from experimental data and further expanded by applying periodic boundary conditions. During each Monte Carlo simulation, 10,000 walkers (electrons) were used and the initial position of electrons was randomly set. By following the variable hopping model, electrons were allowed to hop to all atoms, in which the probability of each hopping event (from islands i to j, P_{ij}) decayed to the exponential of hopping distance (R_{ij}, from islands i to j) by $P_{ij} \propto \exp^{-\alpha R_{ij}}$. Similar to the variable-range-hopping model, the parameter α is set as 1 (see Supplementary Note 4 for more discussion).

Data availability
All related data generated and/or analysed in this study are available from the corresponding author on reasonable request.

Code availability
Code is provided at GitHub (https://github.com/vipandyc/AMC_Monte_Carlo; https://github.com/ningustc/AMCProcessing).

42. Krivanek, O. L. et al. Atom-by-atom structural and chemical analysis by annular dark-field electron microscopy. *Nature* **464**, 571–574 (2010).
43. Kresse, G. & Furthmuller, J. Efficient iterative schemes for *ab initio* total-energy calculations using a plane-wave basis set. *Phys. Rev. B* **54**, 11169–11186 (1996).
44. Kresse, G. & Joubert, D. From ultrasoft pseudopotentials to the projector augmented-wave method. *Phys. Rev. B* **59**, 1758–1775 (1999).
45. Perdew, J. P., Burke, K. & Ernzerhof, M. Generalized gradient approximation made simple. *Phys. Rev. Lett.* **77**, 3865–3868 (1996).
46. Grimme, S., Antony, J., Ehrlich, S. & Krieg, H. A consistent and accurate *ab initio* parametrization of density functional dispersion correction (DFT-D) for the 94 elements H-Pu. *J. Chem. Phys.* **132**, 154104 (2010).

Author contributions L.Liu and H.T. conceived the project. H.T., J.C., W.Z. and L.Liu designed the experiments and calculations. P.-F.Z., K.Z., J.-Y.W., T.L. and J.P. synthesized the molecule precursors. H.T. performed the CVD growth, with assistance from J.Liu, H.T., R.L., P.L., S.Y., S.L., Y.L., X.H., K.L., Y.J., Y.Zhang and Y.Hou performed the Raman, XPS, atomic force microscopy and other general characterizations. X.L., J.W., Z.X., P.G., L.Lin, L.W. and X.B. performed the SAED characterizations. Y.M., S.N., M.X., X.Z., S.J.P. and W.Z. performed the STEM and NBED experiments and data analysis. M.C., E.H., E.W. and J.C. performed the density functional theory calculations and other theoretical calculations. H.T., Z.L., Z.Y., J.G. and W.F. fabricated the device and performed the room-temperature electrical measurements. Y.Zou, D.D., Y.Huang, J.Lu, Y.Han, Z.W. and Z.G.C. performed the low-temperature transport measurements. H.T., M.C., M.L., J.C., W.Z. and L.Liu wrote the paper. All authors discussed and commented on the manuscript.

a

b

c

8.07
8.05
7.80
7.78
−7.26
6.62
6.60
6.58

1.00
1.04
1.04

10.0 9.5 9.0 8.5 8.0 7.5 7.0 6.5 6.0 5.5 5.0 4.5 4.0 3.5 3.0 2.5 2.0 1.5 1.0 0.5 0.0

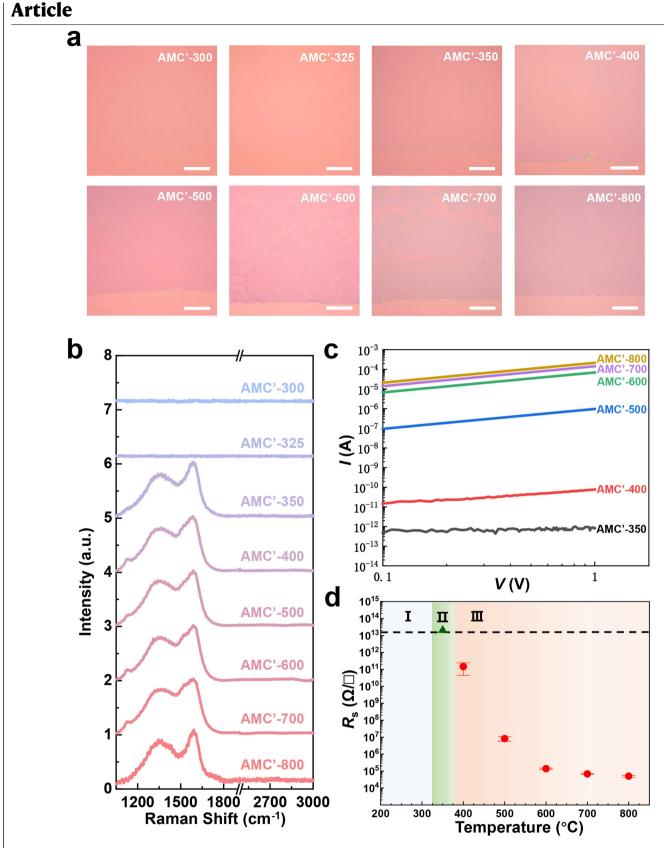**Extended Data Fig. 1 | Molecule synthesis and characterization. a**, Organic synthesis route of BN-doped 1,8-dibromonaphthalene, which was used as the main precursor for the growth. (a) C_3H_5MgBr (2 equiv), 70%; (b) $(Cy_3P)_2Cl_2$ Ru=CHPh (0.8 mol%), CH_2Cl_2, 92%; (c) 2,3-dicyano-5,6-dichlorobenzoquinone (2 equiv), hexane, 60 °C, 17%; (d) $AlBr_3$, *N*-bromosuccinimide, CH_2Cl_2, 62%. **b**, Molecular structure of 1,8-dibromonaphthalene used as the growth precursor in the control experiment. **c**, ¹H nuclear magnetic resonance spectrum of compound **5** (400 MHz, $CDCl_3$, 298 K).
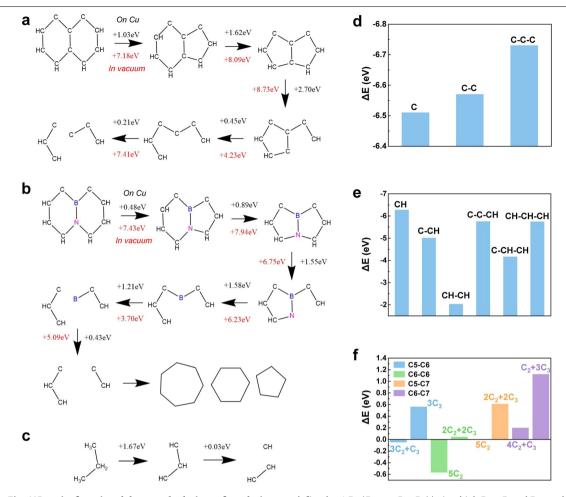
Extended Data Fig. 2 | Characterizations of AMC samples grown at different temperatures. a, Representative optical images of AMC samples, showing the limited coverage at low temperature (275 °C and 300 °C), continuous and uniform films at medium temperatures (325–500 °C) and films with bilayer regions at high temperatures (600–800 °C). **b**, Raman spectra of AMC samples, showing the similar feature, that is, broad D and G peaks without G′ signals. At 850 °C, a weak G′ peak was found at about 2,690 cm⁻¹. **c**, Raman mapping of I_D/I_G for AMC-300, AMC-400 and AMC-500, demonstrating the spatial uniformity. **d**, Statistics of I_D/I_G as a function of growth temperature, showing no monotonic, or apparent, temperature dependence. Considering the DOD differences among AMC samples as shown by STEM characterizations, I_D/I_G is probably not a good indicator of DOD. Scale bars, 200 μm (**a**), 5 μm (**c**).
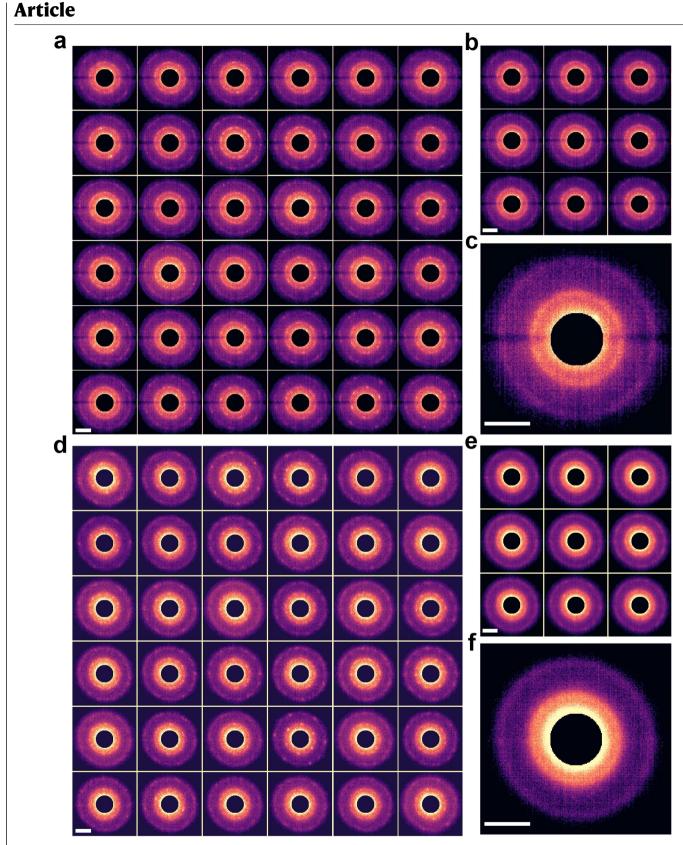
Extended Data Fig. 3 | Characterizations of AMC' samples with 1,8-dibromonaphthalene as the precursors. a, Optical images of AMC' samples transferred onto SiO₂/Si substrates. No AMC' sample was obtained at 300 °C or 325 °C. Continuous and uniform AMC' films were obtained at intermediate temperatures and samples with the continuous first layer and the partially covered second layer were obtained when $T \geq 600$ °C. **b**, Raman spectra of AMC' samples, showing the complete absence of G' peaks. **c**, I–V curves of two-terminal AMC' devices, showing varied conductivities for AMC' samples. **d**, Diagram of R_s as a function of growth temperature, naturally exhibiting three zones. Scale bar, 200 μm (**a**).
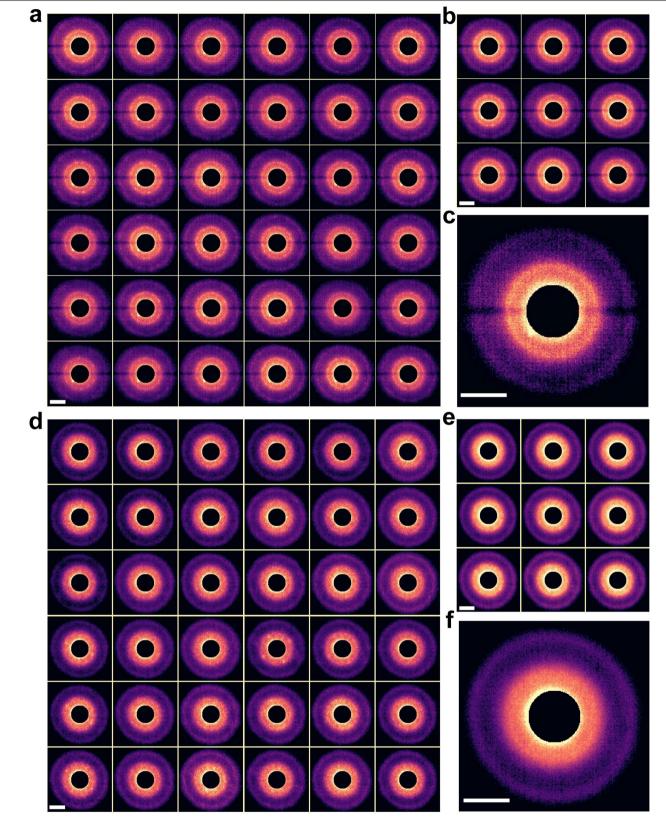
Extended Data Fig. 4 | Density functional theory calculations of catalytic (on Cu) and thermal (in vacuum) cracking of two molecules. a,b, The predicted reaction process and energy profiles of splitting the molecules (without Br) without (**a**) and with (**b**) BN doping into carbon chains. The reaction energy is defined as the energy of the final state minus that of the initial state. **c,** The calculated decomposition route and energy barriers for A_3-2 (CH_3-CH_2-CH_3) cracking on Cu. **d,** The formation energy (ΔE) per carbon atom on the Cu(100) surface for C, C-C and C-C-C. For n carbon atoms, ΔE is defined as $\Delta E = (E_{total} - nE_C - E_{Cu})/n$, in which E_{total}, E_C and E_{Cu} are the energies of the absorbed system, a single carbon atom in vacuum and a Cu surface, respectively. **e,** The absorption energy (ΔE) of C_xH_y species on the Cu(100) surface. The absorption energy ΔE is defined as $\Delta E = (E_{total} - nE_{CxHy} - E_{Cu})/n$. **f,** Reaction enthalpies for 1D linear chains forming 2D compact clusters. $mC_x + nC_y$ on the x label means the combination of m C_x and n C_y carbon chains. C5-C6 (containing nine carbon atoms) represents a pentagon sharing an edge with a hexagon and the same notation applies for C6-C6, C5-C7 and C6-C7.
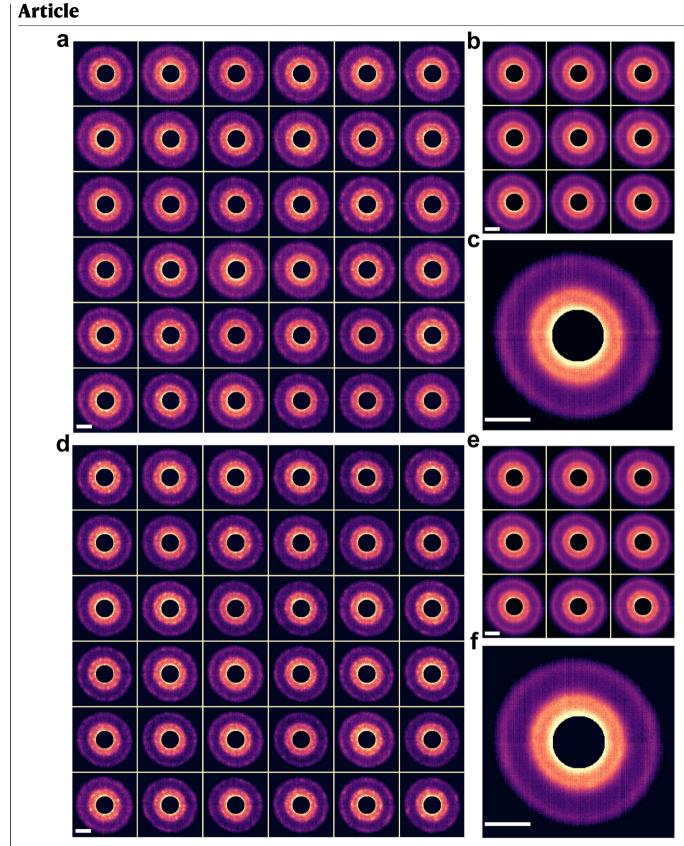
Extended Data Fig. 5 | Region-averaged 4D-STEM NBED patterns of AMC-300 from two different areas, one area with in situ heating (a–c) and one without heating (d–f). The scanning region of the 4D-STEM dataset is 36×36 nm^2. Averaged NBED patterns are obtained by dividing the whole scanning regions into 6×6 (**a**,**d**), 3×3 (**b**,**e**) and 1×1 (**c**,**f**) subregions. The NBED patterns of different subregions in **a** and **d** show strong diffuse halos, along with occasional broadened diffraction spots, demonstrating the random spatial distribution of crystallites and glassy structures at the small scale of 6 nm.

The diffraction spots gradually become broadened and disappear when increasing the size of the averaging region from 6×6 nm^2 (**a**,**d**) to 12×12 nm^2 (**b**,**e**) and 36×36 nm^2 (**c**,**f**), in agreement with the SAED result in Fig. 2a. The results of **a**–**c** were obtained using in situ heating at 650 °C and the dark strips in the centre of convergent-beam electron diffraction patterns are minor gain artefacts from the CMOS camera. The results of **d**–**f** were obtained at room temperature. Scale bars, 5 nm^{-1} (**a**–**f**).
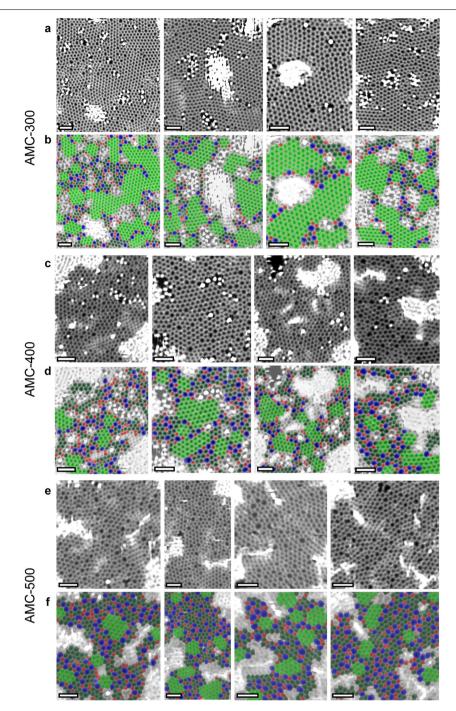
Extended Data Fig. 6 | Region-averaged 4D-STEM NBED patterns of AMC-400 from two different areas, one area with in situ heating (a–c) and one without heating (d–f). The scanning region of the 4D-STEM dataset is 36×36 nm^2. Averaged NBED patterns are obtained by dividing the whole scanning regions into 6×6 (**a**,**d**), 3×3 (**b**,**e**) and 1×1 (**c**,**f**) subregions. Diffuse halos are the dominant features of subregion NBED patterns (**a**,**d**), indicating the distinctive structure difference between AMC-300 (Extended Data Fig. 5) and AMC-400 at the sub-10-nm scale. The halos become more diffuse when increasing the size of the averaging region from 6×6 nm^2 (**a**,**d**) to 12×12 nm^2 (**b**,**e**) and exhibit no apparent difference with AMC-300 and AMC-500 at the scale of 36×36 nm^2 (**c**,**f**). Region-averaged NBED results strongly confirm the greater DOD in AMC-400, consistent with the conclusion from real-space STEM images in the main text. The results of **a**–**c** were obtained using in situ heating at 650 °C and the dark strips in the centre of convergent-beam electron diffraction patterns are minor gain artefacts from the CMOS camera. The results of **d**–**f** were obtained at room temperature. Scale bars, 5 nm^{-1} (**a**–**f**).
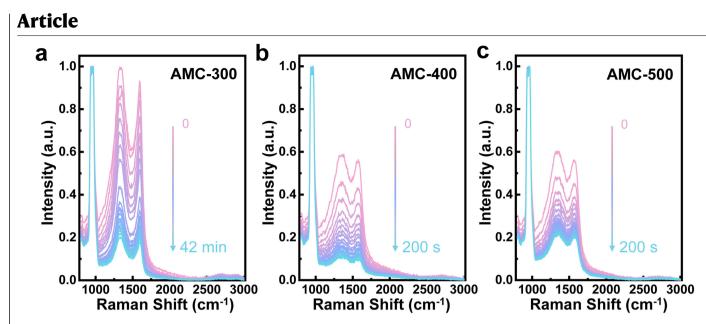
Extended Data Fig. 7 | Region-averaged 4D-STEM NBED patterns of AMC-500 from two different areas, a–c in one area and d–f in the other. The scanning region of the 4D-STEM dataset is 36 × 36 nm^2. Averaged NBED patterns are obtained by dividing the whole scanning regions into 6 × 6 (**a**,**d**), 3 × 3 (**b**,**e**) and 1 × 1 (**c**,**f**) subregions, respectively. Diffuse halos with blurry spots are found as the main features of subregion NBED patterns **a** and **d**, showing the intermediate DOD that agrees with the finding from STEM images. The halos become more diffuse when increasing the size of the averaging region from 6 × 6 nm^2 (**a**,**d**) to 12 × 12 nm^2 (**b**,**e**) and exhibit no apparent difference with AMC-300 and AMC-400 at the scale of 36 × 36 nm^2 (**c**,**f**). The results were obtained at room temperature. Scale bars, 5 nm^{-1} (**a**–**f**).
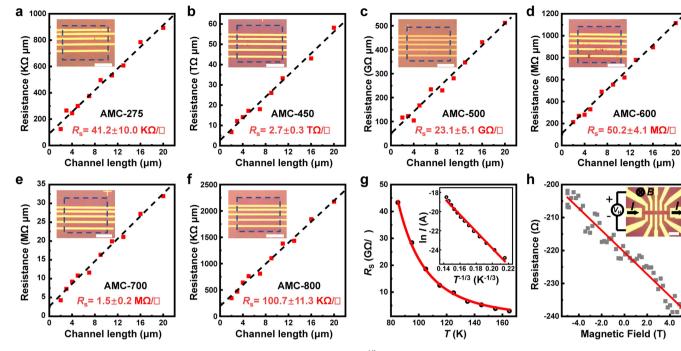
Extended Data Fig. 8 | Denoised ADF-STEM images and the corresponding structural mapping of the AMC-300 (a,b), AMC-400 (c,d) and AMC-500 (e,f) samples, respectively. Pentagons are filled with red. Heptagons and octagons are filled with blue. Hexagons are filled with bright green or dark green to show crystallites or isolated areas, respectively. The results of **a**–**d** were obtained using in situ heating at 650 °C and the results of **e** and **f** were obtained by first annealing the sample at 650 °C for 2 h in the JEOL 2100Plus transmission electron microscope, cooling down to room temperature and quickly transferring into the Nion U-HERMES100 microscope for characterization at room temperature. Scale bars, 1 nm (**a**–**f**).
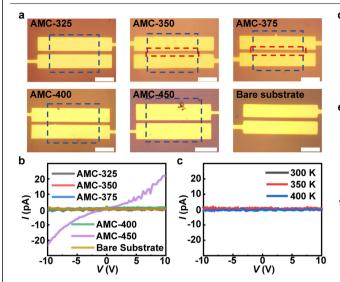
a

b

c

Extended Data Fig. 9 | Thermostability of AMC-300 (a), AMC-400 (b) and AMC-500 samples (c) in air shown by Raman spectroscopy. The monolayers were transferred onto SiO_2/Si substrates and then consecutive Raman measurements were performed by 4 mW of laser (continuous wave, 532 nm). The acquisition time of a single spectrum was 10 s, with the interval duration of 100 s for AM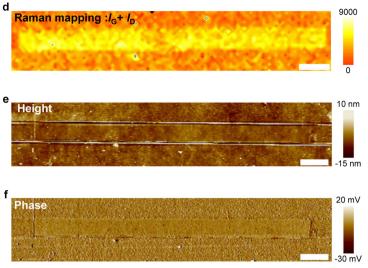C-300 and no breaks for AMC-400 and AMC-500. We noticed that, with longer laser irradiation, the Raman intensities from the same spot gradually decayed owing to the structural damage by the heating effect. By tracing the evolution of Raman spectra, we found that AMC-300 held the highest thermostability, whereas AMC-400 suffered severely from the radiolysis. The results of the thermostability evaluation are consistent with our atomic-level structure characterizations.

Extended Data Fig. 10 | Electrical measurements of conductive AMC samples. a–f, Measurements of R_s by the TLM for AMC samples in zones II and IV, showing the temperature-dependent conductivities. Insets, optical images of as-fabricated devices. **g**, R_s (black circles) as a function of T in one device of AMC in zone IV (550 °C). Inset, natural logarithm of the current as a function of $T^{1/3}$. The red lines are the fits to the 2D variable-range-hopping model. **h**, Results of room-temperature Hall measurements, showing the p-type semiconductor behaviour with a mobility of about 0.1 cm^2 V^{-1} S^{-1}. Inset, optical image of the device with the standard Hall bar configuration. Scale bars, 20 μm (insets of **a–f**,**h**).

Article

Extended Data Fig. 11 | Electrical measurements of insulating AMC samples.
a, Optical images of as-fabricated AMC devices with the sample highlighted by dashed blue lines. **b**, Two-terminal I–V curves with a bias sweep from −10 V to 10 V. AMC samples from zone III, including AMC-325, AMC-350, AMC-375 and AMC-400, show <2 pA of the current, comparable with that from the bare SiO$_2$ substrate, strongly suggesting the highly insulating behaviours. By contrast, AMC-450 from zone IV manifests an almost linear current response. We note that we treat this I–V curve of AMC-450 (the normal linear response to applied voltage but with the lowest current in all AMC devices) as the detection limit of our instruments for the AMC system. **c**, Temperature-dependent I–V curves for AMC-350, showing no increase of the current at elevated temperatures.

d, Raman mapping of the sum of G and D peaks (in area), corresponding to the channel region of the AMC-350 device marked by the dashed red lines in the top-middle panel of **a**, demonstrating the continuity of AMC across two electrodes. **e**,**f**, Atomic force microscopy results of the AMC-375 channel area (indicated by the dashed red line in the top-right panel of **a**) in height (**e**) and phase (**f**), both showing the absence of any apparent structural cracks or holes. By confirming the AMC continuity in the device channel from the Raman and atomic force microscopy characterizations, we conclude that AMC samples from zone III are indeed electrically insulating with the comparable level with SiO$_2$, or at least in the limit of our instruments. Scale bars, 20 μm (**a**), 5 μm (**d**–**f**).